Ionization calculations using classical molecular dynamics

Daniel Plummer [1,*] Pontus Svensson [1] Dirk O. Gericke [2] Patrick Hollebon [3]
Sam M. Vinko [1,4] and Gianluca Gregori [1]

[1]*Department of Physics, University of Oxford OX1 3PU, United Kingdom*
[2]*Centre for Fusion, Space and Astrophysics, Department of Physics, University of Warwick, Coventry CV4 7AL, United Kingdom*
[3]*AWE, Aldermaston, Reading, Berkshire RG7 4PR, United Kingdom*
[4]*Central Laser Facility STFC Rutherford Appleton Laboratory, Didcot OX11 0QX, United Kingdom*

(Received 2 September 2024; accepted 3 January 2025; published 13 January 2025)

By performing an ensemble of molecular dynamics simulations, the model-dependent ionization state is computed for strongly interacting systems self-consistently. This is accomplished through a free energy minimization framework based on the technique of thermodynamic integration. To illustrate the method, two simple models applicable to partially ionized hydrogen plasma are presented in which pair potentials are employed between ions and neutral particles. Within the models, electrons are either bound in the hydrogen ground state or distributed in a uniform charge-neutralizing background. Particular attention is given to the transition between atomic gas and ionized plasma, where the effect of neutral interactions is explored beyond commonly used models in the chemical picture. Furthermore, pressure ionization is observed when short-range repulsion effects are included between neutrals. The developed technique is general, and we discuss the applicability to a variety of molecular dynamics models for partially ionized warm dense matter.

DOI: 10.1103/PhysRevE.111.015204

I. INTRODUCTION

Accurate evaluation of the properties of matter in the warm dense state presents a formidable challenge for both theoretical and computational techniques. Strong ionic coupling hinders analytical calculations, while the accurate treatment of quantum-mechanical electrons severely restricts the system size accessible to first-principles calculations. A common heuristic for the first of these two properties is the classical Coulomb coupling parameter, which is associated with the ratio of average potential energy to average kinetic energy and, for a fully ionized system, takes the form,

$$\Gamma = \frac{Z^2 e^2}{4\pi\epsilon_0 a}\frac{1}{k_B T}, \tag{1}$$

where the charge state of the ions is Z, the system is at temperature T, k_B is Boltzmann's constant and ϵ_0 is the dielectric constant. The Wigner-Seitz radius $a = (4\pi n/3)^{-1/3}$ is an approximate measure of the interparticle separation and depends on the ionic number density n. Strong coupling implies $\Gamma \gtrsim 1$. The prominence of quantum statistical effects is quantified with the degeneracy parameter,

$$\theta = \frac{k_B T}{E_F}, \tag{2}$$

which is the ratio of average kinetic energy to Fermi energy E_F of the system. Partial degeneracy means the electron kinetic energy is comparable to the Fermi energy, $\theta \sim 1$. Furthermore, partial ionization, where electrons populate both bound and free states, can occur in warm dense matter (WDM) and is the focus of the current work. For further discussion on the parameters relevant to WDM, see Ref. [1].

A large range of computational and theoretical methods have been applied to WDM [1,2]. Quantum statistical computations such as path integral Monte Carlo can access a host of observables, but are hampered by the so-called fermionic sign problem and are limited to relatively small system size [1–4]. In molecular dynamics (MD) approaches, the nuclei are commonly treated as classical point particles, while the electron subsystem can be treated to different levels of approximation. Typically, an adiabatic assumption is invoked such that the electron kinetics are decoupled from the ionic motion and in first-principles schemes, the thermal electron distribution is often evaluated in the density functional theory framework [1,2,5]. Alternatively, simple one-component plasma (OCP) models can be employed where electrons are incorporated in effective ion-ion potentials, derived from a model dielectric response [6–8]. In the original OCP [9–15], the electrons are assumed to form a uniform charge-neutralizing background and the ions interact through the bare Coulomb potential. The simplicity the OCP approximations allows simulations of millions of particles [16], and equilibrium properties have been well characterized by many authors, e.g., Refs. [9,10,17,18]. Semiclassical MD models have also been applied to WDM, which include a dynamic representation of the electrons, and therefore simulate the two-component plasma (TCP). Prevalent approaches include wave packet molecular dynamics [19–25], quantum statistical

*Contact author: daniel.plummer@physics.ox.ac.uk

potentials [26–29], and Bohmian approaches [30,31]. Both OCP and TCP models employ representations of free or weakly bound electrons.

To correctly evaluate the bulk properties of WDM in atomistic simulations, large systems are often required. For example, many particles are needed to characterise transport behavior in the hydrodynamic limit [18,32–34]. Therefore, to extend OCP and TCP methods to partially ionized materials, while retaining the computational efficiency necessary to access substantial system sizes, a chemical picture may be required. In this framework each ionic charge state is considered as a distinct species with appropriate interparticle potentials, such that the equilibrium charge state distribution must be known to compute both dynamic and static equilibrium properties. Importantly, the distribution will depend on the model being used, so it must be computed in a self-consistent framework. Ebeling and Militzer attempted such a calculation for a hydrogen plasma wavepacket model by performing simulations to minimize the internal energy as a function of ionization state at constant entropy, however, their approach assumes an ideal entropy term and is therefore limited to weak coupling [21]. In the same work, transitions between bound and free populations were also considered, for which the equilibrium ionization state becomes an important benchmark. A chemical picture MD approach could also provide a useful reference for TCP modeling strategies that incorporate bound states dynamically such as those discussed in Refs. [29,35].

In parallel to the development of MD methods, a rich literature exists surrounding both analytical and semiempirical models in the chemical picture [4,36–44]. These models consider distinct chemical species and typically perform variational free energy calculations to obtain their equilibrium value. Various approximations exist, but interatomic repulsive interactions are usually treated on the level of hard spheres, which exclude the volume accessible to other species. The chemical picture is also applied to predict x-ray scattering spectra of dense plasmas through the Chihara decomposition [2,45]. Furthermore, the ionization state is generally a key property in the hydrodynamic and spectroscopic modeling of plasmas [46–49].

Given these motivations, the current paper is devoted to computing exact model-dependent ionization states directly from MD, an approach we do not believe has previously been employed. Specifically, we consider a simple system, which is applicable to partially ionized hydrogen and perform a set of excess free energy computations to determine the self-consistent equilibrium ionization state in the presence of strong coupling. Furthermore, the generalization to materials with higher atomic numbers is straightforward, provided that realistic interparticle potentials are supplied. To calculate free energies we devise a framework based on the thermodynamic integration (TI) technique [50]. The paper consists of three core sections. In Sec. II, two models applicable to partially ionized hydrogen plasma are introduced. Following this, in Sec. III, we develop a free energy minimization framework to compute the ionization state of a given model. Section IV details the application of this framework and presents results for the computed ionization states over a range of densities. Finally, conclusions are drawn in Sec. V.

II. HYDROGEN MODELS

We consider a partially ionized and charge-neutral coulomb system in a box of volume $V = L^3$. The box is subject to periodic boundary conditions and contains N electrons, and an equal number of protons. A chemical picture is employed, where free electrons form a uniform background charge, and each bound electron is spatially localized on a specific ion. The system may therefore be partitioned into N_i ions and N_n neutrals, such that $N = N_i + N_n$. The general expression for the Hamiltonian used in the MD simulations is

$$\mathcal{H}^{(\mathrm{MD})} = \sum_k^{N_\mathrm{i}} \frac{\left(\mathbf{p}_k^\mathrm{i}\right)^2}{2m_\mathrm{i}} + \sum_l^{N_\mathrm{n}} \frac{\left(\mathbf{p}_l^\mathrm{n}\right)^2}{2m_\mathrm{n}} + \mathcal{U}^{(\mathrm{MD})}, \tag{3}$$

where m_i is the ion mass, and the neutral mass $m_\mathrm{n} = m_\mathrm{i} + m_\mathrm{e}$ is the sum of electron and ion masses. The momentum of the kth ion is $\mathbf{p}_k^\mathrm{i}$ and the lth neutral is $\mathbf{p}_l^\mathrm{n}$. The potential energy function $\mathcal{U}^{(\mathrm{MD})}$ determines the interactions of the system and depends on the configuration of the particles—modifications to this function serve as the central object for the thermodynamic integration computation given in Sec. III A. In the following sections, the potentials used to model the particle interactions are introduced.

A. Bound state Coulomb model

In the first model considered, which is referred to as the bound state Coulomb (BSC) model, each bound electron is modeled as a frozen single-particle wavefunction given by (atomic units are used unless otherwise specified):

$$\psi_{1\mathrm{s}}(\mathbf{x}) = \frac{1}{\sqrt{\pi}} \exp\left(-|\mathbf{x}|\right), \tag{4}$$

which is equivalent to the ground state of an isolated hydrogen atom, up to a global phase. A neutral particle is configured by superposing the electron onto an ion at position $\mathbf{r}_l^\mathrm{n}$ giving access to the charge density of a single neutral,

$$\rho^\mathrm{n}\left(\mathbf{x}, \mathbf{r}_l^\mathrm{n}\right) = \delta^3\left(\mathbf{x} - \mathbf{r}_l^\mathrm{n}\right) - \left|\psi_{1\mathrm{s}}\left(\mathbf{x} - \mathbf{r}_l^\mathrm{n}\right)\right|^2. \tag{5}$$

The subscript index l labels a given neutral particle. Alternatively, in the ionized case, the ion at position $\mathbf{r}_k^\mathrm{i}$ and corresponding free electron can be combined to give the charge density of a pseudo-ion:

$$\rho^\mathrm{i}\left(\mathbf{x}, \mathbf{r}_k^\mathrm{i}\right) = \delta^3\left(\mathbf{x} - \mathbf{r}_k^\mathrm{i}\right) - 1/V. \tag{6}$$

Similarly, the subscript index k labels a pseudo-ion particle. The interactions are written in terms of the pseudo-ion, such that the electron background acts to modify the heavy-particle interactions. In this section, we henceforth consider the system to be composed of N_n neutrals and N_i pseudoions with charge distributions given by Eqs. (5) and (6), respectively. To compute the potential of the system, Poisson's equation is solved for these charge distributions, subject to periodic boundary conditions. Specifically, the ion-neutral (in) and neutral-neutral (nn) interaction potentials are computed with,

$$U^{\mathrm{in/nn}}\left(\left|\mathbf{r}_k^{\mathrm{i/n}} - \mathbf{r}_l^\mathrm{n}\right|\right) = \int_V \int_V \frac{\rho^{\mathrm{i/n}}\left(\mathbf{x}, \mathbf{r}_k^{\mathrm{i/n}}\right)\rho^\mathrm{n}\left(\mathbf{x}', \mathbf{r}_l^\mathrm{n}\right)}{|\mathbf{x} - \mathbf{x}'|} d\mathbf{x}' d\mathbf{x}, \tag{7}$$

which acts between distinct particles. The model admits short range pair potentials, which are a function of the radial distance r between particles and determine the neutral dynamics,

$$U^{\rm in}_{\rm pair}(r) = \frac{e^{-2r}}{r}(1+r), \tag{8}$$

$$U^{\rm nn}_{\rm pair}(r) = \frac{e^{-2r}}{r}\left(1+\frac{5}{8}r-\frac{3}{4}r^2-\frac{1}{6}r^3\right). \tag{9}$$

These potentials resemble those used in Ref. [21], and the neutral interactions are screened on the length scale of the bound states, as expected. There is also a volume-dependent contribution from the neutrals interacting with the free electron background charge,

$$U^{\rm in}_0 = -\frac{2\pi N_{\rm i} N_{\rm n}}{V}, \tag{10}$$

which directly arises from computing $U^{\rm in}$ in Eq. (7). To ease the presentation of the TI method in Sec. III A the total interaction energy between different species are explicitly defined. The total energy between pseudo-ions and neutrals is

$$V_{\rm in} = U^{\rm in}_0 + \sum_{k,l}\sum_{\mathbf{n}} U^{\rm in}_{\rm pair}\left(|\mathbf{r}^{\rm i}_k - \mathbf{r}^{\rm n}_l + \mathbf{n}L|\right), \tag{11}$$

where the first sum over k, l is over all ion-neutral pairs and the second sum is over the vector of integers $\mathbf{n} = (n_x, n_y, n_z) \in \mathbb{Z}^3$. The total neutral-neutral energy is similarly given by the following double summation over neutral positions,

$$V_{\rm nn} = \frac{1}{2}\sum_{l,m}{\sum_{\mathbf{n}}}' U^{\rm nn}_{\rm pair}\left(|\mathbf{r}^{\rm n}_l - \mathbf{r}^{\rm n}_m + \mathbf{n}L|\right). \tag{12}$$

The prime notation indicates that $\mathbf{n} = (0,0,0)$ term is omitted for $l = m$, i.e., there is no self interaction in the central box, but particles do interact with their own periodic images. The factor of one half in Eq. (12) corrects for double counting.

B. OCP interactions

The remaining component are the pseudo-ion interactions which form a one-component plasma (OCP) subsystem and can be similarly decomposed as pair and constant terms [9,13,51]. The pair potential

$$U^{\rm ii}_{\rm pair}(\mathbf{r}) = v_1(\mathbf{r}) + v_2(\mathbf{r}) \tag{13}$$

is computed under the Ewald method and therefore split into two convergent summations [52]. The first term represents real space contributions to the energy and is given by

$$v_1(\mathbf{r}) = \sum_{\mathbf{n}} \frac{\mathrm{erfc}(g|\mathbf{r}+\mathbf{n}L|)}{|\mathbf{r}+\mathbf{n}L|}, \tag{14}$$

where g is the Ewald parameter, chosen to optimize numerical performance [53], and $\mathrm{erfc}(\cdot)$ is the complementary error function. The second term in Eq. (13) represents reciprocal space contributions to the pairwise energy,

$$v_2(\mathbf{r}) = \frac{1}{V}\sum_{\mathbf{k}\neq 0}\frac{4\pi}{k^2}e^{-k^2/4g^2}\cos(\mathbf{k}\cdot\mathbf{r}), \tag{15}$$

and runs over nonzero k vectors where $\mathbf{k} = 2\pi\mathbf{n}/L$. Furthermore there is a constant energy contribution comprized of four terms [13],

$$U^{\rm ii}_0 = \frac{N_i}{2}\sum_{\mathbf{n}\neq 0}\frac{\mathrm{erfc}(gnL)}{\mathbf{n}L} + \frac{N_i}{2}\sum_{\mathbf{k}\neq 0}\frac{4\pi}{k^2}e^{-k^2/4g^2} - N_{\rm i}\frac{g}{\sqrt{\pi}} - N_{\rm i}^2\frac{\pi}{2g^2V}. \tag{16}$$

The OCP interactions fully account for the ion-background and background-background contributions of the model [9]. Generally, the presence of the uniform free electron background provides a regularization to the ion-ion interactions, which would otherwise formally diverge, and contributes a finite energy offset to all inter-species potentials involving pseudo-ions, e.g., Eq. (10). These constant energy terms do not affect the dynamics but do depend on the number of particles, and therefore are particularly relevant for comparing free energies at different ionization states. Similarly, electron background energy contributions have been discussed in the context of phase diagram calculations [8]. The total OCP energy consists of the constant term and a sum over pairs of pseudo-ions,

$$V_{\rm ii} = U^{\rm ii}_0 + \sum_{j<k} U^{\rm ii}_{\rm pair}\left(|\mathbf{r}^{\rm i}_j - \mathbf{r}^{\rm i}_k|\right). \tag{17}$$

The OCP pair potential has the periodic boundary conditions included and therefore no sum over periodic images is required, in contrast to Eqs. (11) and (12).

C. Short-range repulsion model

In plasma models that apply a chemical picture, hard-sphere potentials are often used, either as a reference potential with known properties, e.g., Ref. [36], or directly, e.g., Ref. [42]. The justification of this second class of potentials is left to Sec. IV B. To investigate an analogous effect, we introduce a second model involving a short-range repulsion (SRR) between neutral particles, noting that similar potentials have been previously introduced to model bound electron repulsion effects for partially ionized plasmas [54,55]. A third potential,

$$U^{\rm nn}_{\rm SRR} = \epsilon\left(\frac{1}{r}\right)^{12}, \tag{18}$$

is applied in combination with the BSC model, that acts solely between neutral pairs. In Eq. (18), ϵ is the overall constant determining the strength of the interaction and is set by equating $U^{\rm nn}_{\rm SRR}(2r_*) = (3/2)k_BT$, to give an effective radius r_*. The total energy due to SRR interactions is

$$V_{\rm SRR} = \sum_{l<m}{\sum_{\mathbf{n}}}' U^{\rm nn}_{\rm SRR}\left(|\mathbf{r}^{\rm n}_l - \mathbf{r}^{\rm n}_m + \mathbf{n}L|\right), \tag{19}$$

where the sum runs over all pairs of neutral particles. The potentials discussed thus far have been implemented as a new pairstyle into the LAMMPS codebase [56], in which all subsequent simulations are performed. The MD potential is given by

$$\mathcal{U}^{(\rm MD)} = V_{\rm ii} + V_{\rm in} + V_{\rm nn} + V_{\rm SRR}, \tag{20}$$

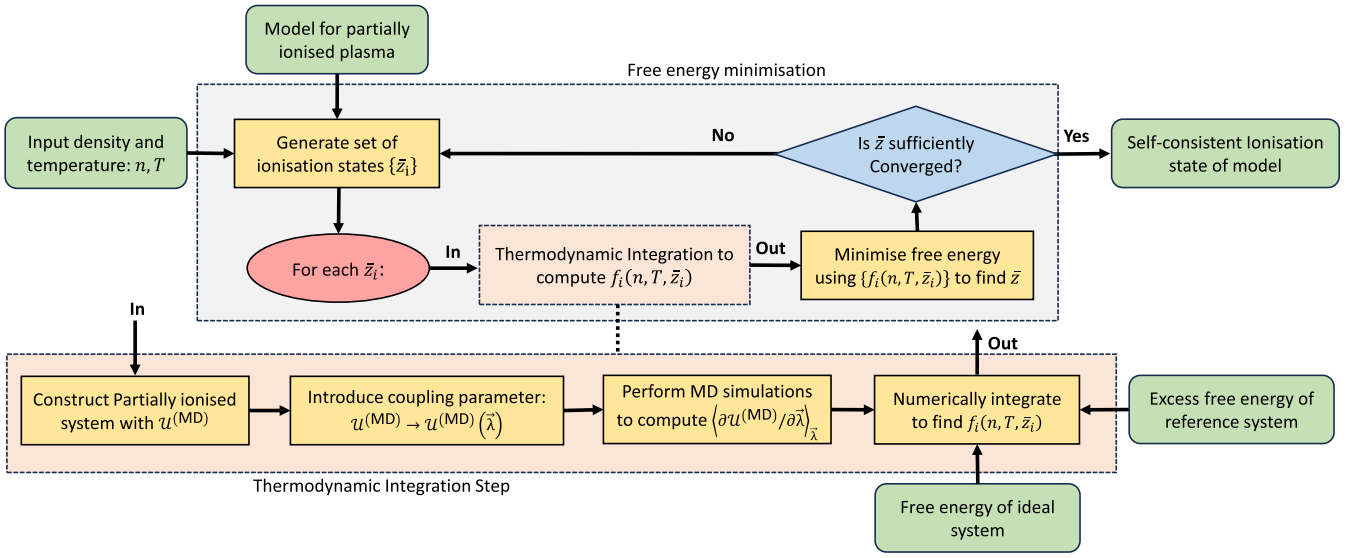

FIG. 1. Schematic depicting the free energy minimization framework, including the thermodynamic integration step (enlarged pink box). The framework requires external input to the calculation (green boxes) and a set of computation steps (yellow boxes), while the red oval represents an iteration over ionization states and the blue diamond a decision. The output is the self-consistent ionization state of the input model, which is also given in a green box. The schematic applies to both models presented in the text, where for the SRR model, the reference system is chosen to be the BSC model.

where for the BSC model, the SRR term is discarded, or equivalently, $\epsilon = 0$. Having defined the two hydrogen models, the ionization calculation methodology will now be introduced.

III. FREE ENERGY MINIMIZATION FRAMEWORK

In any model that distinguishes between bound and free electrons, the ionization state is key quantity of interest. In hydrogenic systems, the ionization state takes a particularly simple form as the ratio of the number of ions to the total number of electrons $\bar{z} = N_\mathrm{i}/N$. A system in thermodynamic equilibrium and held at constant density $n = N/V$ and temperature T will exhibit a minimum in the Helmholtz free energy:

$$\left(\frac{\partial f}{\partial \bar{z}}\right)_{n,T} = 0. \tag{21}$$

Equation (21) is valid under the constraint of charge neutrality and $f = F/Nk_BT$ is the reduced free energy per particle. The equilibrium ionization state may therefore be found by computing the free energy across a set of artificial ionization states and performing a minimization procedure. These considerations apply to any chemical picture of hydrogen, and are readily generalizable to heavier elements [38,39,57], where different charge states will be present. We employ this approach in MD applications where, given a set of interparticle potentials, the effect of strong coupling can be treated exactly. The methodology to compute the free energy is detailed in the following section.

A. Thermodynamic integration

The Helmholtz free energy depends on the accessible volume of the underlying phase space, and is not directly accessible in MD simulations. For this reason, we have performed a multistep thermodynamic integration (TI) to compute the free energy across different ionization states [50]. A coupling vector $\vec{\lambda}$ may be introduced into the MD potential,

$$\mathcal{U}^{(\mathrm{MD})} \to \mathcal{U}^{(\mathrm{MD})}(\vec{\lambda}) \tag{22}$$

in a currently unspecified manner. Two important cases are imposed: When the coupling vector is the null vector, $\vec{\lambda} = \vec{0}$, the system is noninteracting (ideal) and when the coupling vector is the unit vector, $\vec{\lambda} = \vec{1}$, the interactions match the those of the model, i.e., the interactions of the target system. The introduction of coupling parameters allows the excess free energy to be written as an integral over ensemble averages evaluated over different coupling strengths [50]:

$$f^{\mathrm{ex}}(n,T,\bar{z}) = \frac{1}{Nk_BT}\int_{\vec{0}}^{\vec{1}} d\vec{\lambda}\cdot\left\langle\frac{\partial\mathcal{U}^{(\mathrm{MD})}(\vec{\lambda})}{\partial\vec{\lambda}}\right\rangle_{\vec{\lambda}}. \tag{23}$$

The notation $\langle\cdot\rangle_{\vec{\lambda}}$ denotes an ensemble average computed for a system at the given coupling vector. In the context of MD, this consists of evaluating time averages over trajectories generated by the Hamiltonian of the system with the potential interactions modified by the coupling vector. Given these trajectories, the components of the vector defined by $\partial\mathcal{H}/\partial\vec{\lambda}$ may be evaluated over them. Therefore a set of simulations are required to numerically evaluate the integral for each ionization state. A schematic for the full minimization framework is presented in Fig. 1, including the TI step. Given that Eq. (23) computes the excess free energy for a set of particle interactions the ideal free energy of the model is required as input for the calculation.

B. Ideal free energy

In line with the BSC model, each hydrogen atom is in its spin-degenerate ground state with binding energy $I \approx$

13.59 eV. Free electrons have two spin states and follow Fermionic statistics. Given that the ideal system is noninteracting, the free energy of the individual species combine linearly,

$$f^{\mathrm{id}}(n,T,\bar{z}) = f_i^{\mathrm{id}} + f_e^{\mathrm{id}} + f_n^{\mathrm{id}}, \tag{24}$$

where the free energy of the ions f_i^{id} and neutrals f_n^{id} are, respectively,

$$f_i^{\mathrm{id}} = \bar{z}\log\left[\bar{z}n\Lambda_i^3\right] - \bar{z}, \tag{25}$$

$$f_n^{\mathrm{id}} = \bar{x}\log\left[\frac{1}{2}\bar{x}n\Lambda_n^3\right] - \bar{x}\frac{I}{k_BT} - \bar{x}, \tag{26}$$

where Λ_α is the thermal de Broglie wavelength of the species α and $\bar{x} = 1 - \bar{z}$ is the neutral fraction. The electrons follow a Fermi-Dirac distribution over free particle states, and their ideal free energy is given by

$$f_e^{\mathrm{id}} = -\frac{2}{3}\frac{\mathcal{F}_{3/2}(\eta_e)}{\mathcal{F}_{1/2}(\eta_e)} + \eta_e, \tag{27}$$

where $\eta_e = \mu_e/k_BT$ is the reduced chemical potential and $\mathcal{F}_j$ is a Fermi-Dirac integral of order j. The chemical potential is computed through the normalization condition $\mathcal{F}_{1/2}(\eta_e) = \bar{z}n\Lambda_e^3/2$. On application of the free energy minimization condition, Eq. (21), to the ideal free energy, Eq. (24), the ideal Saha equation can be recovered in the limit where the free electrons are nondegenerate, $\theta \ll 1$. Further details are given in Appendix A. There are different avenues by which excited atomic states could be included within the calculation, either by assuming a parameterized distribution of states in the atom, and modifying the interaction accordingly, or introducing each excited state as another independent species. These extensions pose no fundamental problems to the calculation, but increase the complexity, and are beyond the scope of the current paper.

C. Bound state Coulomb model free energy calculation

To compute the free energy of the BSC model, two coupling parameters $\vec{\lambda} = (\lambda_1, \lambda_2)$ are introduced into the MD potential. The first entry λ_1 controls the strength of pseudo-ion interactions, while λ_2 modifies all neutral interactions such that

$$\mathcal{U}^{(\mathrm{MD})}(\vec{\lambda}) = \lambda_1 V_{\mathrm{ii}} + \lambda_2(V_{\mathrm{in}} + V_{\mathrm{nn}}). \tag{28}$$

The intermediate state $\vec{\lambda} = (1, 0)$ constitutes an ideal gas of neutrals immersed in an interacting OCP. Given that extensive equation of data exists for the OCP it serves as the reference system for the calculation, with free energy f^{OCP}, which solely depends on the effective coulomb coupling parameter, which itself is a function of the ionization state, density, and temperature. We provide our own parametrization of data from Caillol [11,12], specified in Appendix B. The OCP data involves integrating over a weakly coupled system with long-range potentials, where the Debye length is necessarily larger than the box size. In this case, the finite-size error is sizable and many more particles have to be used to estimate the interaction energy in the thermodynamic limit [12], further discussion is given in Appendix B. By using the OCP as the reference system in the calculation, we overcome these issues in a computationally efficient manner. To compute the free energy of the target system, $f^{\mathrm{BSC}}(n, T, \bar{z})$, we evaluate,

$$f^{\mathrm{BSC}} = f^{\mathrm{OCP}} + \frac{1}{Nk_BT}\int_0^1 d\lambda_2 \langle V_{\mathrm{in}} + V_{\mathrm{nn}}\rangle_{(1,\lambda_2)}, \tag{29}$$

which follows from equation (23), over different ionizations states.

D. Short-range repulsion free energy calculation

To compute the free energy of the SRR model, a third coupling parameter is introduced that controls the strength of the additional repulsive interactions,

$$\mathcal{U}^{(\mathrm{MD})}(\vec{\lambda}) = \lambda_1 V_{\mathrm{ii}} + \lambda_2(V_{\mathrm{in}} + V_{\mathrm{nn}}) + (\lambda_3)^{12} V_{\mathrm{SRR}}. \tag{30}$$

Introducing this parameter to the power of 12, mirroring the dependence of the SRR potential, Eq. (18), on radial separation, avoids singularities when evaluating the ensemble average of $\partial V_{\mathrm{SRR}}/\partial\lambda_3$ [58]. The free energy is calculated by a natural extension of formula (23), where the BSC model now acts as the reference system:

$$f^{\mathrm{SRR}} = f^{\mathrm{BSC}} + \frac{1}{Nk_BT}\int_0^1 d\lambda_3 \langle 12\lambda_3^{11} V_{\mathrm{SRR}}\rangle_{(1,1,\lambda_3)}, \tag{31}$$

which is an application of Eq. (23) where the coupling vector now has three entries $\vec{\lambda} = (\lambda_1, \lambda_2, \lambda_3)$. Computational expense is reduced by choosing the reference system as the BSC model, in which there are already soft repulsive interactions present. The TI method benefits from having similar reference and target systems, such that fewer coupling parameter points are needed to accurately resolve the TI curve and estimate the integral in Eq. (23) [59].

IV. SIMULATION RESULTS

In this section simulation results pertaining to the computation of the ensemble averages in Eqs. (29) and (31) are presented. The subsequent free energy minimization and ionization calculation are also given and discussed. All simulations were performed for a constant temperature $T = 62500\ \mathrm{K} \approx 5.38\ \mathrm{eV}$ across a range of densities $r_s = a/a_B = \{4, 3, 2, 1.5, 1, 0.75, 0.5\}$ where a_B denotes the Bohr radius. These conditions were selected because at this temperature, molecule formation between hydrogen atoms is unlikely while partial ionization is predicted to occur [4,27]. Ionization states were chosen in an iterative scheme to sample the minima in free energy. In each simulation $N = 1024$ heavy particles were initialized from a configuration that minimized the potential energy, thermalized for 2.5 ps to the target temperature by applying a velocity rescaling every 0.5 fs, before trajectory data was collected over 5 ps. For both models, statistics were then gathered over six independent runs, and used to produce the thermodynamic integration curves discussed below. This procedure ensures that different local configurations of the canonical ensemble are sampled. Finite-size tests were carried out and confirmed sufficient convergence with respect to system size with a relevant example given in Appendix C. At high densities, $r_s \leqslant 0.75$, convergence was not reached for the BSC model at low ionization states. This corresponds to

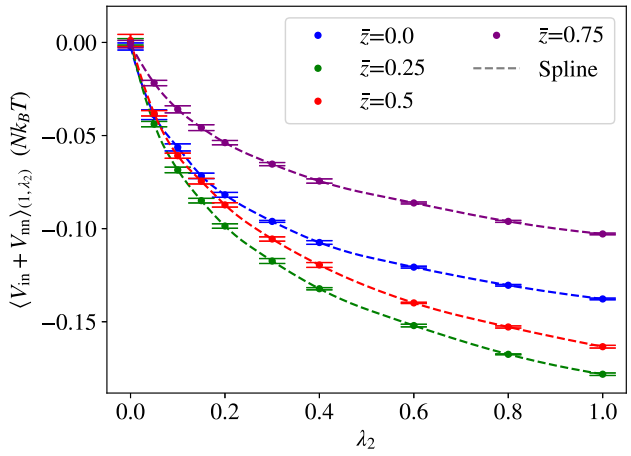

FIG. 2. Thermodynamic integration curves for the BSC model at $r_s = 2$, the integrand in Eq. (29) is plotted for different values of λ_2. For clarity, a subset of ionization states are displayed. The data was averaged over six independent runs, while error bars are the corresponding standard deviations.

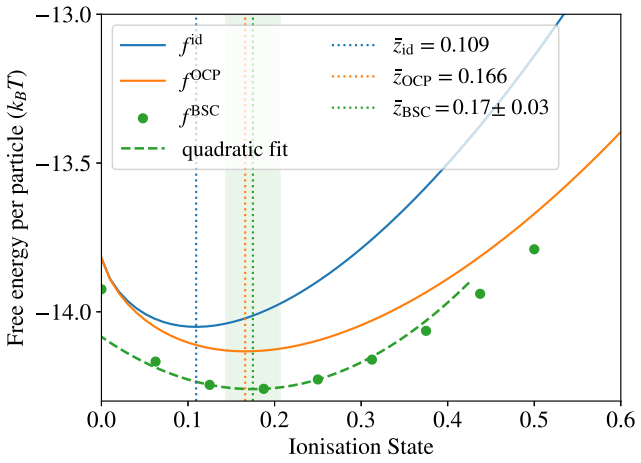

FIG. 3. BSC Model free energy minimization for $r_s = 2$. The curves with solid lines correspond to free energies of the ideal (blue, $\vec{\lambda} = \vec{0}$), reference (orange, $\vec{\lambda} = (1, 0)$), and target (purple, $\vec{\lambda} = \vec{1}$) system, while the dotted lines show their minima, the uncertainty in the quadratic minimization is also displayed in the green shaded rectangle. The corresponding values of these minima are given in the legend.

a breakdown of the model and further discussion is provided in Sec. IV C.

A. Free energy minimization of bound state Coulomb model

Example thermodynamic integration curves are given in Fig. 2, where results are shown for $r_s = 2$ and selected ionization states. At $\lambda_2 = 0$, all curves start at zero. The neutral trajectories are uncorrelated and therefore sample an integral over the ion-neutral and neutral-neutral potentials, both of which integrate to zero over the box. In the literature this condition is often used to set the zero of energy in periodic systems [60,61], a convention followed here. As λ_2 increases, the curves exhibit an initial sharp decrease, before entering a linear regime. Furthermore, for small λ_2, the fluctuations in the ensemble averages are larger. Both effects are caused by trajectories passing close by one another due to the weak interactions. This results in large fluctuations in the magnitude of the potentials when evaluated over these paths, but with sufficient averaging this effect is reduced, as demonstrated in Fig. 2, where the corresponding errors are small. A spline is fit to each curve and integrated to find the free energy with Eq. (29). Given that the spline fitting is less accurate in regions of larger curvature, the integrand is sampled at finer resolution for lower coupling parameters to provide a more accurate calculation of the free energy. A discussion of the error associated to the integrand sampling is also given in Appendix C.

Figure 3 shows the corresponding free energy curves for the BSC model, where all sampled ionization states are included. The ideal case and reference systems are also plotted, which are parameterized functions and are readily minimized. A finite set of data are available to minimize the neutral free energy, and therefore a quadratic curve is fit to the lowest three data points to extract the minima. The error mainly depends upon the resolution in ionization state, which we estimate to be half the interval over which the quadratic curve is fitted. When including the OCP interactions, the collective binding energy between the ions and free electron background lowers the free energy at higher ionization states. Therefore, the ionization state that minimizes the free energy increases. Only ion screening is present and the inclusion of an electronic response would cause further increase, as there are additional negative free energy contributions due to screening [62]. The attractive Coulomb interactions increasing the ionization state is a form of ionization potential depression, and corresponds to a lowering of the energy difference between the bound state and the continuum, a connection, which is asserted in Appendix A. At $\bar{z} = 0$, the OCP and ideal systems have the same free energy, given that no ions are present.

The BSC interactions further lower the magnitude of free energy, and the net effect produces a small positive shift in the ionization state. The decrease in energy is caused by binding between neutrals and the background and the negative asymptote in the neutral-neutral interaction. The latter is the reason for the decrease in free energy at $\bar{z} = 0$ while at $\bar{z} = 1$ the free energies of the target and reference system necessarily agree. The repulsive effects present in the potentials at small interparticle distances contribute to the small increase in ionization.

B. Including short-range repulsion effects

Hard-sphere potentials have been used many times within the chemical picture literature as computational devices [4,36–39,41–44]. The charge-neutral interaction in this approach simply restricts the volume accesible to charged species, which is an analytically tractable mechanism and has therefore found prevalent use. For example, Saumon and Chabrier found that, at high densities, the free energy of their model was lower when fully neutral compared to when fully ionized [36]. Given that the system was expected to be fully pressure ionized, an additional hard-sphere potential was introduced between neutral species with radius $2a_0$. Although

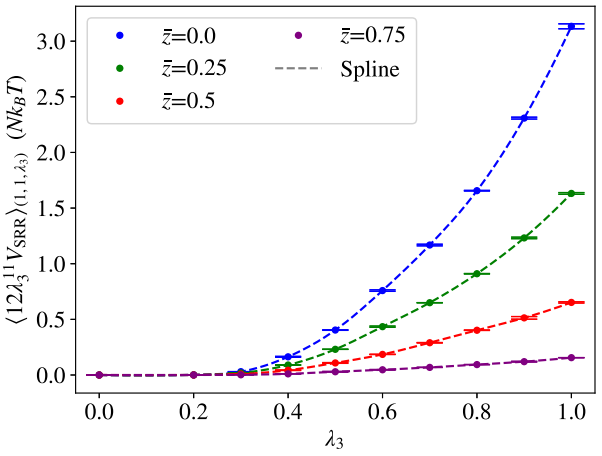

FIG. 4. Thermodynamic integration curves for $r_s = 2$ corresponding to the introduction of short-range repulsion into the BSC model. For clarity, a subset of ionization states are displayed. The data was averaged over six independent runs, while error bars are the corresponding standard deviations.

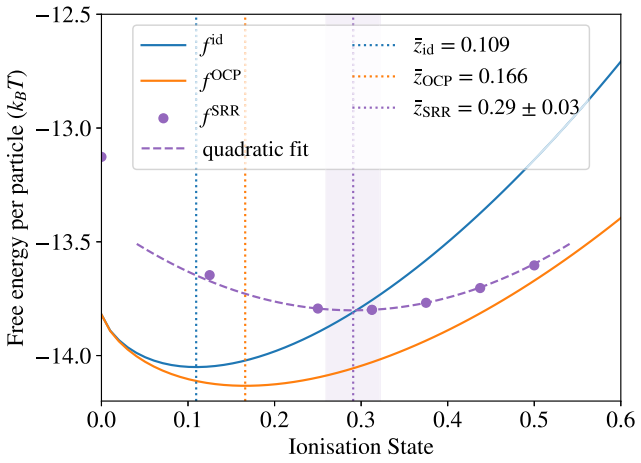

FIG. 5. SRR model free energy minimization at $r_s = 2$. The curves with solid lines correspond to free energies of the ideal (blue, $\vec{\lambda} = \vec{0}$), reference [orange, $\vec{\lambda} = (1, 1, 0)$], and target (purple, $\vec{\lambda} = \vec{1}$) system, while the dotted lines show their minima, the uncertainty in the quadratic minimization is also displayed in the purple shaded rectangle. The corresponding values of these minima are given in the legend.

the model presented here does not include the same framework of internal atomic states, or interatomic interactions, we still observe the same phenomenon. Along similar lines, Potekhin introduced an additional unbinding free energy to account for the inner-core screening effect of overlapping atomic orbitals [44]. Furthermore, in many models in the chemical picture, neutral species interaction effects are modeled directly as hard spheres [4,41,42].

Given these motivations, and as a demonstration of the technique, an additional SRR potential (as described in Sec. II C) with effective radius $r_* = 1$ has been introduced into the neutral-neutral interaction to study its effect on the predicted ionization state. We note that such a potential could also be used to model Pauli exclusion effects between bound electrons [54,55]—these are already treated exactly in the ideal free electron gas but are not present in bound-bound or bound-free interactions. The appropriate form of the repulsive potential is unknown, but could possibly be deduced through comparison with high-fidelity data, sourced from experiment or first-principles computations. Alternatively, a scheme based on the pairwise Pauli interactions from wave packet molecular dynamics could be devized [19,25]. A third integration is required evaluate the influence of the harder interneutral core on the ionization state. A characteristic integration curve is given in Fig. 4 where all curves are suppressed for small λ_3 by the factor of $(\lambda_3)^{11}$ in the derivative of the potential energy function. The free energies for this condition are displayed in Fig. 5. The increased atomic repulsion drives the free energy at lower ionization states up, causing an increase in the minima. The free energy remains below the OCP free energy for higher ionization states (not shown in figure) due to the attractive neutral-background contributions.

C. Ionization state across density

The minimization results from the simulations performed with both the BSC model and SRR model are compiled in Fig. 6. The ionization state of the ideal hydrogen plasma decreases with increasing density. This is because the density of free particle states decreases and it becomes energetically favorable to reduce the effective number of species. Including the OCP interactions turns on long-range charged-particle interactions and increases the ionization state, as discussed in Sec. IV A. As r_s decreases, the Coulomb coupling parameter is larger, which means the negative excess free energy contributions are greater, and the system exhibits larger bind-

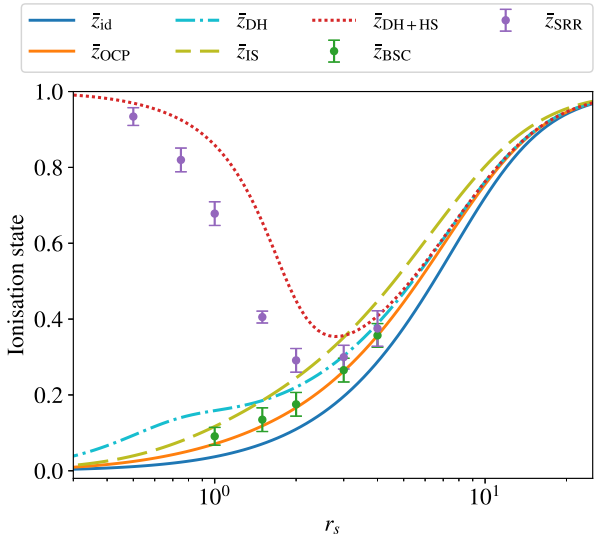

FIG. 6. Ionization states for models discussed in the main text plotted against r_s. The BSC model (green) and SRR model (purple) correspond to results from numerically minimizing free energy data. The solid curves correspond to the ideal case (blue) and OCP reference system (orange). The remaining lines relate to the free energy models defined in Appendix D.

ing between the ions and electron background, encouraging ionization. At the highest densities, $r_s \leqslant 1$, the free electron degeneracy contributions are dominant and the ionization state still tends to zero. Common models for the OCP interactions are the Debye-Hückel and ion-sphere models, which, when inserted into the minimization procedure, give $\bar{z}_{\mathrm{DH}}$ and $\bar{z}_{\mathrm{IS}}$, respectively. The models are defined in Appendix D. When compared with the OCP reference calculation, both models overpredict the ionization state. The Debye-Hückel model is correct in the weak coupling limit, and therefore good agreement is found for $r_s \gtrsim 5$. The ion-sphere model is more appropriate in the strongly coupled (high-density) regime, where it outperforms the Debye-Hückel prediction when compared against the more accurate OCP prediction. Generally, the overprediction for both models is severe, considering that the magnitude of deviation is similar to the difference between ideal and OCP curves. The deviation is directly related to both models overestimating the magnitude of the excess internal energy, which can be seen in Fig. 7.

We now discuss the effect of introducing neutral interactions, starting with the BSC model introduced in Sec. II A. For $r_s \gtrsim 4$, the Coulomb interactions of the neutrals have a negligible effect and the deviation in ionization from the ideal case is purely driven by OCP interactions in the plasma. As the density increases, neutral interactions induce a small increase in the ionization state. This is an effect of the ion-neutral and neutral-neutral repulsion effects. At the two highest densities considered: $r_s = 0.5$ and $r_s = 0.75$, and for high neutral fractions, the neutral-ion mixture separated into a dense ball of neutral particles surrounded by ions, hence breaking the isotropy of the fluid. This phase separation is another indication that the interneutral potential is too weak and these points are omitted from Fig. 6. We note that at higher ionization states, this effect is not present, and allows the BSC system to be used as an appropriate reference system when performing integration calculations with the SRR potential.

Finally, the effect of increasing the strength of collisions between neutrals has a large effect in the high-density region, as expected. The pressure ionization transition is recovered, because portions of the neutral-neutral potential that were attractive are now repulsive. This illustrates that interaction-induced ionization is due to both long-range Coulomb interactions and short-range repulsive interactions. For pressure ionization to occur an additional repulsive interaction was artifically introduced, suggesting that effects beyond frozen-core Coulomb interactions are required when modeling bound states in dense plasmas. By minimizing a Debye-Hückel model for the ions combined with a hard-sphere equation of state for the neutrals, the $\bar{z}_{\mathrm{DH+HS}}$ curve is produced. Further details are given in Appendix D. There is qualitative agreement between this model and the full SRR model. However a limited treatment of the OCP energy, neglect of the ion-neutral interaction, and replacement of the SRR potential by hard spheres results in an overestimation of the ionization state at high densities.

V. CONCLUSION

Molecular dynamics has a large flexibility in the choice of interparticle potential and is accurate at arbitrarily strong coupling. Meanwhile, for plasmas, the interparticle potentials are closely connected to the ionization state. Therefore, the presented thermodynamic integration technique provides the possibility to extend existing models that use the chemical picture. It is also essential to determine the self-consistent ionization state within molecular dynamics itself for models that involve chemical formulations such as quantum statistical potentials and wave packet molecular dynamics, which was the primary motivation for this study. Furthermore, we have investigated the ionization state dependence on the interplay between ionic screening and neutral repulsion in hydrogen. The excluded-volume method has been used in all chemical-picture-based models of dense plasmas thus far to evaluate repulsive interaction effects. Given that the presented method applies to arbitrary interaction potentials, we make the first step beyond this paradigm with the bound state Coulomb and short-range repulsion models.

The results presented from the one component models provide stimulus for improvement. For example, free electron interaction effects can be included either in effective ion-ion potentials [6,8,63], or in two-component models [25]. Free electrons provide additional screening and therefore would further lower the free energy at higher ionization states [62], causing the equilibrium ionization state to increase. Meanwhile, multispecies systems with excited states and multiple charge states can be included within the minimization framework. On including these developments, and leveraging the presented ionization state calculation framework, comparison could be made against hydrogen equation-of-state tables [2].

Generally, the development of models in the chemical picture could be particularly useful in developing computational frameworks for ionization potential depression (IPD) [2], given that known models falter at strong coupling [49], and that IPD is nontrivial to extract from first-principles computations [64–67]. In the results presented, an IPD effect is present, and dominated by ion-ion Coulomb interactions at lower densities. Furthermore, molecular dynamics provides a promising route to ionic transport coefficients, provided reliable interparticle potentials are supplied.

ACKNOWLEDGMENTS

We thank Thomas Campbell and Thomas Gawne for insightful discussions. We are grateful for the use of computing resources provided by STFC Scientific Computing Department's SCARF cluster, where all simulations for this work were carried out. D.P., P.S., S.M.V., and G.G. acknowledge support from AWE-NST UK via Oxford Centre for High Energy Density Science (OxCHEDs). PS acknowledges funding from the Oxford Physics Endowment for Graduates (OXPEG). S.M.V. acknowledges support from the UK EPSRC Grant No. EP/W010097/1. The work of S.M.V. and G.G. has received partial support from EPSRC and First Light Fusion under the AMPLIFI Prosperity partnership, Grant No. EP/X025 373/1.

APPENDIX A: SAHA EQUATION

The Saha equation is a common formulation used to determine the charge state distribution in partially ionized

plasma [2,38]. In this Appendix, it is demonstrated how the free energy minimization procedure reduces to a hydrogenic Saha equation, such that the interactions can therefore be characterized as IPD. The total free energy of the system is the sum of ideal and excess contributions:

$$f = f^{\mathrm{id}} + f^{\mathrm{ex}}. \tag{A1}$$

Additionally, for illustrative purposes, the chemical potential of the electrons may be expressed as

$$\mu_e = k_B T \log\left(\frac{\bar{z} n \Lambda_e^3}{2}\right) + \Delta\mu_e, \tag{A2}$$

where the first term is the contribution in the nondegenerate limit, and $\Delta\mu_e$ corrects for degeneracy. On applying the free energy minimization, Eq. (21) and using the ideal free energy of the models, Eq. (24), the following relation can be obtained:

$$\frac{\bar{z}^2 n}{(1-\bar{z})} = \left(\frac{\Lambda_n}{\Lambda_i \Lambda_e}\right)^3 \exp\left(-\frac{I + \Delta\mu_e - \Delta I}{k_B T}\right), \tag{A3}$$

where ΔI is defined as

$$\Delta I = -k_B T \frac{\partial f^{\mathrm{ex}}}{\partial \bar{z}}. \tag{A4}$$

In the ideal ($\Gamma \ll 1$) and nondegenerate ($\theta \gg 1$) limits: $f^{\mathrm{ex}} = \Delta\mu_e = 0$, and Eq. (A3) is equivalent to a common form of the hydrogenic Saha equation [38]. Furthermore this form allows two distinct physical effects related to the ionization state to be isolated by identifying the effective ionization potential [2],

$$I^{\mathrm{eff}} = I + \Delta\mu_e - \Delta I. \tag{A5}$$

The average energy of an electron in a Fermi gas is larger than that in a classical gas, because lower-lying energy states are blocked through the Pauli principle. This means that $\Delta\mu_e > 0$ and the effective ionization potential is increased. This corresponds to more energy being required to ionise a bound electron. Lastly, the presence of interactions modifies the effective ionization potential through ΔI, which can be identified as IPD. Similar expressions have been used previously to quantify IPD [68,69]. Inspecting Eq. (A4), shows that this quantity acts to reduce the ionization potential when the excess free energy decreases with increasing ionization. Both the OCP and SRR interactions fall into this category. As mentioned in Sec. V, our method gives direct access to the IPD and could be exploited for this purpose. We emphasise that the fidelity of the result ultimately depends upon the choice of interparticle potentials which determine the excess free energy f^{ex}.

APPENDIX B: PARAMETERIZATION OF OCP DATA

On application of Eq. (23), the free energy due to interactions of the OCP system is found through

$$f^{\mathrm{ex}}_{\mathrm{OCP}}(n, T, \bar{z}) = \frac{1}{N k_B T} \int_0^1 \langle V_{\mathrm{ii}} \rangle_{(\lambda_1, 0)} d\lambda_1. \tag{B1}$$

The integral is simply equal to the excess free energy of an OCP at an effective coupling parameter $\Gamma^{\mathrm{eff}} = \bar{\Gamma}(\bar{z}n, T)$, and Eq. (B1) may be written [9,10,12],

$$f^{\mathrm{ex}}_{\mathrm{OCP}}(\Gamma^{\mathrm{eff}}) = \bar{z} \int_0^{\Gamma^{\mathrm{eff}}} \frac{u^{\mathrm{ex}}_{\mathrm{OCP}}(\Gamma)}{\Gamma} d\Gamma, \tag{B2}$$

where $u^{\mathrm{ex}}_{\mathrm{OCP}} = U^{\mathrm{ex}}/N_i k_B T$ is the excess internal energy per particle of the OCP at a given coupling parameter, in units of $k_B T$. We performed a parametrization of OCP internal energy data from Monte Carlo simulations by Caillol [11,12], which are well resolved in the weakly coupled limit. A finite-size correction scheme is also applied in these works. The functional form,

$$u^{\mathrm{ex}}_{\mathrm{OCP}} = \Gamma^{3/2}\left[\frac{A_1}{\sqrt{\Gamma + A_2}} + \frac{A_3}{\Gamma + 1}\right] + \frac{B_1 \Gamma^2}{\Gamma + B_2} + \frac{B_3 \Gamma^2}{\Gamma^2 + B_4}, \tag{B3}$$

from Ref. [70] was fitted to the data, which includes the asymptotic Debye-Hückel limit of the OCP equation of state. The fitting constants are given in Table I and $A_3 = -\sqrt{3}/2 - A_1/\sqrt{A_2}$.

TABLE I. Coefficient values for the functional form paramterizing the excess OCP energy.

A_1	A_2	B_1	B_2	B_3	B_4
–0.99787	0.77480	0.093431	1.5534	0.036253	4.1379

In Fig. 7 the excellent agreement is shown across a wide range of Coulomb coupling, the largest differences to the parametrizations given in Ref. [70] are for weak coupling, where, in this work, there is additional data for low coupling from Ref. [12]. Although we note that these discrepancies are small, this regime is relevant to the overall free energy calculation because it is integrated over. The functional form allowed simple and fast evaluation of the free energy of the

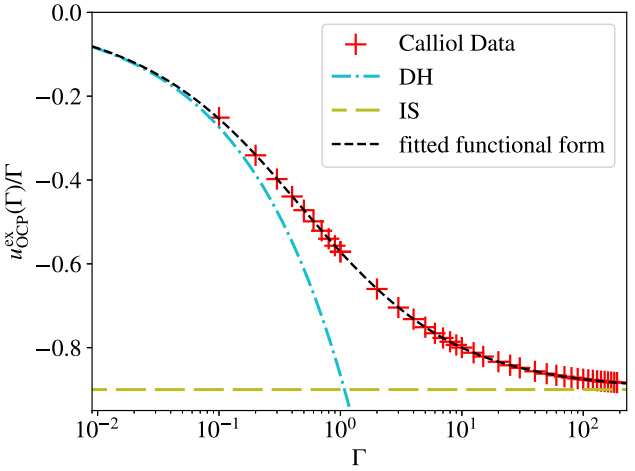

FIG. 7. Thermodynamic Integration curve (black dashed line) used for the reference system in this work. The functional form from Ref. [70] is fitted to OCP data from Refs. [11,12] given by the red plus symbols. The Debye-Hückel (DH) and ion-sphere (IS) models which are defined in Appendix D are plotted for comparison.

reference system, which was found by performing the integral in Eq. (B2) analytically [70]:

$$\begin{aligned} f^{\rm ex}_{\rm OCP}(\Gamma) = & A_1\sqrt{\Gamma(A_2+\Gamma)} \\ & + A_1A_2\log(-\sqrt{\Gamma/A_2}+\sqrt{1+\Gamma/A_2}) \\ & + 2A_3[\sqrt{\Gamma}-\arctan\sqrt{\Gamma}] \\ & + B_1\left[\Gamma - B_2\log\left(1+\frac{\Gamma}{B_2}\right)\right] \\ & + \frac{B_3}{2}\log\left(1+\frac{\Gamma^2}{B_4}\right), \end{aligned} \tag{B4}$$

where the boundary condition $f^{\rm OCP}(0)=0$ has been applied. There is a small discrepency between line 4 in Eq. (B4) and the equivalent term in Ref. [70], which we assume is due to a misprint in the latter, while the remaining terms formally agree.

APPENDIX C: FINITE-SIZE TESTS

Various finite-size tests were performed to check the convergence of the thermodynamic integration calculation. In this section we present the a finite-size study of the free energy calculation for an ionization state of $\bar{z}=0.5$ and density of $r_s=1$ with the BSC model. Different numbers of heavy particles ranging from $N=128$ to $N=4096$ were used. To maintain a fixed density, the cubic box was rescaled accordingly with box lengths ranging from $L\approx 8.12\,a_B$ to $L\approx 25.8\,a_B$. TI curves were generated for each case with the same resolution in coupling parameter as used in Fig. 2. Each curve was then integrated to find the free energy. To calculate the statistical error in the final excess free energy, separate splines were fit to the points given by the upper and lower error bars and integrated accordingly, to give the upper and lower bounds plotted in Fig. 8. The statistical error is small for all cases, and decreases with system size. This is because, for larger systems, there are more trajectories to sample the integrand in Eq. (29). The systematic error due to system size is also low, and the results are well converged for 2^{10} particles, the number used for all results shown in the main text. Given that the TI errors are rather small, approximately $5\times10^{-3}\,k_BT$ in this case, we assume the error in the full ionization state calculation is mainly due to having a finite number of free energy data points to minimize.

APPENDIX D: IONIZATION MODELS

In Sec. IV C, comparison is made against simpler models, which are defined in this Appendix. Here they are presented as models for the excess free energy, but may be converted to an expression for IPD with Eq. (A4). The first two models are concerned with the excess OCP contributions to the free energy, linked to the excess internal energy through Eq. (B2). The Debye-Hückel (DH) model accounts for ionic screening in the weakly coupled limit [12,15] and is given by

$$f^{\rm ex}_{\rm DH} = -\bar{z}^{3/2}\frac{\Gamma^{3/2}}{\sqrt{3}}. \tag{D1}$$

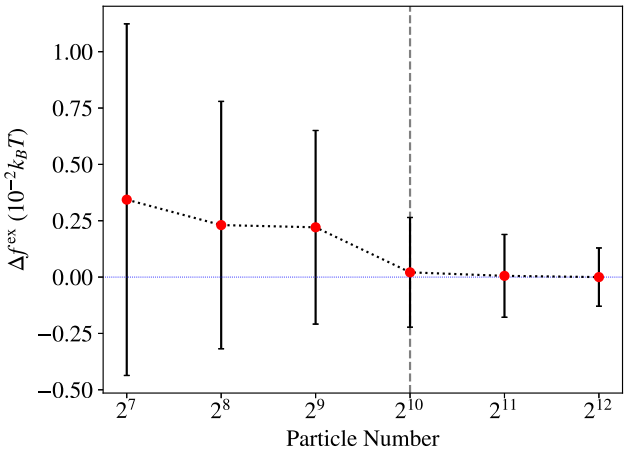

FIG. 8. Excess free energy of the BSC model computed for different numbers of particles at a fixed density of $r_s=1$ and ionization state of $\bar{z}=0.5$ in units of $10^{-2}k_BT$. The results are shown relative to the result for $N=2^{12}$ particles: $f^{\rm ex}_{\rm BSC}\approx-0.7124$. The dashed gray line indicates the number of particles used for the results in the main text.

Alternatively the ion-sphere (IS) model may be used, which formally provides a lower bound on the excess internal energy, as seen in Fig. 7, and is applicable in the strongly coupled limit [14,15]. The following expression is used,

$$f^{\rm ex}_{\rm IS} = -\bar{z}^{4/3}\frac{9\Gamma}{10}. \tag{D2}$$

For the IS model, integration over the weakly coupled limit introduces a substantial error in the OCP free energy. Therefore alternative reference systems have been suggested in the literature by employing external data [14]. However, to be consistent with commonly used IS models, e.g., Ref. [41], Eq. (D2) is used in this work.

Both DH and IS models apply to the OCP subsystem and don't include neutral interactions. To estimate the effect of neutrals, the Carnahan-Stirling equation of state may be utilized [71]. Neutrals interacting through the SRR potential with the effective radius r_* may, in a simple approximation, be modeled as hard spheres of radius $R=r_*$. In the model, the excess free energy due to hard-sphere interactions is

$$f^{\rm ex}_{\rm HS} = \bar{x}\frac{4\eta-3\eta^2}{(1-\eta)^2}, \quad \eta = 2\pi\bar{x}nR^3. \tag{D3}$$

Here η is the packing fraction, and, as before, $\bar{x}$ is the neutral fraction. Finally, to estimate the effect of ion and neutral interactions simultaneously, the DH and HS free energy terms may be combined linearly, the minima of which is given by $\bar{z}_{\rm DH+HS}$ in Fig. 6. As mentioned in the main text, this discards the effect of ion-neutral interactions.

[1] M. Bonitz, T. Dornheim, Z. A. Moldabekov, S. Zhang, P. Hamann, H. Kählert, A. Filinov, K. Ramakrishna, and J. Vorberger, *Ab initio* simulation of warm dense matter, Phys. Plasmas **27**, 042710 (2020).

[2] M. Bonitz, J. Vorberger, M. Bethkenhagen, M. P. Böhme, D. M. Ceperley, A. Filinov, T. Gawne, F. Graziani, G. Gregori, P. Hamann, S. B. Hansen, M. Holzmann, S. X. Hu, H. Kählert, V. V. Karasiev, U. Kleinschmidt, L. Kordts, C. Makait, B. Militzer, Z. A. Moldabekov *et al.*, Phys. Plasmas **31**, 110501 (2024).

[3] T. Dornheim, S. Groth, and M. Bonitz, The uniform electron gas at warm dense matter conditions, Phys. Rep. **744**, 1 (2018).

[4] A. V. Filinov and M. Bonitz, Equation of state of partially ionized hydrogen and deuterium plasma revisited, Phys. Rev. E **108**, 055212 (2023).

[5] D. Marx and J. Hutter, *Ab Initio Molecular Dynamics: Basic Theory and Advanced Methods* (Cambridge University Press, Cambridge, 2009).

[6] Z. A. Moldabekov, S. Groth, T. Dornheim, H. Kählert, M. Bonitz, and T. S. Ramazanov, Structural characteristics of strongly coupled ions in a dense quantum plasma, Phys. Rev. E **98**, 023207 (2018).

[7] Z. A. Moldabekov, H. Kählert, T. Dornheim, S. Groth, M. Bonitz, and T. S. Ramazanov, Dynamical structure factor of strongly coupled ions in a dense quantum plasma, Phys. Rev. E **99**, 053203 (2019).

[8] S. Blouin and J. Daligault, Direct evaluation of the phase diagrams of dense multicomponent plasmas by integration of the clapeyron equations, Phys. Rev. E **103**, 043204 (2021).

[9] S. G. Brush, H. L. Sahlin, and E. Teller, Monte Carlo study of a one-component plasma. I, J. Chem. Phys. **45**, 2102 (1966).

[10] J. P. Hansen, Statistical mechanics of dense ionized matter. I. equilibrium properties of the classical one-component plasma, Phys. Rev. A **8**, 3096 (1973).

[11] J. M. Caillol, Thermodynamic limit of the excess internal energy of the fluid phase of a one-component plasma: A Monte Carlo study, J. Chem. Phys. **111**, 6538 (1999).

[12] J.-M. Caillol and D. Gilles, An accurate equation of state for the one-component plasma in the low coupling regime, J. Phys. A: Math. Theor. **43**, 105501 (2010).

[13] A. S. Onegin, G. S. Demyanov, and P. R. Levashov, Pressure of Coulomb systems with volume-dependent long-range potentials, J. Phys. A: Math. Theor. **57**, 205002 (2024).

[14] S. A. Khrapak and A. G. Khrapak, Simple thermodynamics of strongly coupled one-component-plasma in two and three dimensions, Phys. Plasmas **21**, 104505 (2014).

[15] M. Baus and J.-P. Hansen, Statistical mechanics of simple Coulomb systems, Phys. Rep. **59**, 1 (1980).

[16] G. S. Demyanov and P. R. Levashov, One-component plasma of a million particles via angular-averaged ewald potential: A Monte Carlo study, Phys. Rev. E **106**, 015204 (2022).

[17] H. Kählert, Thermodynamic and transport coefficients from the dynamic structure factor of Yukawa liquids, Phys. Rev. Res. **2**, 033287 (2020).

[18] J. P. Mithen, J. Daligault, and G. Gregori, Extent of validity of the hydrodynamic description of ions in dense plasmas, Phys. Rev. E **83**, 015401(R) (2011).

[19] D. Klakow, C. Toepffer, and P.-G. Reinhard, Hydrogen under extreme conditions, Phys. Lett. A **192**, 55 (1994).

[20] D. Klakow, C. Toepffer, and P. Reinhard, Semiclassical molecular dynamics for strongly coupled Coulomb systems, J. Chem. Phys. **101**, 10766 (1994).

[21] W. Ebeling and B. Militzer, Quantum molecular dynamics of partially ionized plasmas, Phys. Lett. A **226**, 298 (1997).

[22] M. Knaup, P.-G. Reinhard, and C. Toepffer, Wave packet molecular dynamics simulations of hydrogen near the transition to a metallic fluid, Contrib. Plasma Phys. **39**, 57 (1999).

[23] Y. Lavrinenko, P. R. Levashov, D. V. Minakov, I. V. Morozov, and I. A. Valuev, Equilibrium properties of warm dense deuterium calculated by the wave packet molecular dynamics and density functional theory method, Phys. Rev. E **104**, 045304 (2021).

[24] R. A. Davis, W. A. Angermeier, R. K. T. Hermsmeier, and T. G. White, Ion modes in dense ionized plasmas through nonadiabatic molecular dynamics, Phys. Rev. Res. **2**, 043139 (2020).

[25] P. Svensson, T. Campbell, F. Graziani, Z. Moldabekov, N. Lyu, V. S. Batista, S. Richardson, S. M. Vinko, and G. Gregori, Development of a new quantum trajectory molecular dynamics framework, Philos. Trans. R. Soc. A **381**, 20220325 (2023).

[26] J. P. Hansen and I. R. McDonald, Microscopic simulation of a hydrogen plasma, Phys. Rev. Lett. **41**, 1379 (1978).

[27] A. V. Filinov, V. O. Golubnychiy, M. Bonitz, W. Ebeling, and J. W. Dufty, Temperature-dependent quantum pair potentials and their application to dense partially ionized hydrogen plasmas, Phys. Rev. E **70**, 046411 (2004).

[28] W. Ebeling, A. Filinov, M. Bonitz, V. Filinov, and T. Pohl, The method of effective potentials in the quantum-statistical theory of plasmas, J. Phys. A: Math. Gen. **39**, 4309 (2006).

[29] A. Calisti, S. Ferri, C. Mossé, and B. Talin, Classical molecular dynamic codes for hot dense plasmas: The bingo code suite, High Energy Density Phys. **50**, 101084 (2024).

[30] B. Larder, D. O. Gericke, S. Richardson, P. Mabey, T. G. White, and G. Gregori, Fast nonadiabatic dynamics of many-body quantum systems, Sci. Adv. **5**, eaaw1634 (2019).

[31] T. Campbell, P. Svensson, B. Larder, D. Plummer, S. M. Vinko, and G. Gregori, A molecular dynamics framework coupled with smoothed particle hydrodynamics for quantum plasma simulations, arXiv:2408.03693.

[32] P. Svensson, Y. Aziz, T. Dornheim, S. Azadi, P. Hollebon, A. Skelt, S. M. Vinko, and G. Gregori, Modelling of warm dense hydrogen via explicit real time electron dynamics: Dynamic structure factors, Phys. Rev. E **110**, 055205 (2024).

[33] M. Schörner, H. R. Rüter, M. French, and R. Redmer, Extending *ab initio* simulations for the ion-ion structure factor of warm dense aluminum to the hydrodynamic limit using neural network potentials, Phys. Rev. B **105**, 174310 (2022).

[34] P. Svensson, P. Hollebon, D. Plummer, S. M. Vinko, and G. Gregori, Modelling of warm dense hydrogen via explicit real time electron dynamics: Electron transport properties, arXiv:2410.08664.

[35] M. A. Gigosos, D. González-Herrero, N. Lara, R. Florido, A. Calisti, S. Ferri, and B. Talin, Classical molecular dynamics simulations of hydrogen plasmas and development of an analytical statistical model for computational validity assessment, Phys. Rev. E **98**, 033307 (2018).

[36] D. Saumon and G. Chabrier, Fluid hydrogen at high density: Pressure ionization, Phys. Rev. A **46**, 2084 (1992).

[37] H. Juranek and R. Redmer, Self-consistent fluid variational theory for pressure dissociation in dense hydrogen, J. Chem. Phys. **112**, 3780 (2000).
[38] W. Ebeling, V. E. Fortov, and V. Filinov, *Quantum Statistics of Dense Gases and Nonideal Plasmas* (Springer, Berlin, 2017).
[39] C. Winisdoerffer and G. Chabrier, Free-energy model for fluid helium at high density, Phys. Rev. E **71**, 026402 (2005).
[40] A. E. Davletov, Y. V. Arkhipov, Y. S. Mukhametkarimov, L. T. Yerimbetova, and I. M. Tkachenko, Generalized chemical model for plasmas with application to the ionization potential depression, New J. Phys. **25**, 063019 (2023).
[41] G. Zimmerman and R. More, Pressure ionization in laser-fusion target simulation, J. Quant. Spectrosc. Radiat. Transfer **23**, 517 (1980).
[42] W. Ebeling, H. Hache, and M. Spahn, Thermodynamics of ionization and dissociation in hydrogen plasmas including fluctuations and magnetic fields, Eur. Phys. J. D **23**, 265 (2003).
[43] D. Hummer and D. Mihalas, The equation of state for stellar envelopes. I - an occupation probability formalism for the truncation of internal partition functions, Astrophys. J. **331**, 794 (1988).
[44] A. Y. Potekhin, Ionization equilibrium of hot hydrogen plasma, Phys. Plasmas **3**, 4156 (1996).
[45] J. Chihara, Difference in x-ray scattering between metallic and non-metallic liquids due to conduction electrons, J. Phys. F **17**, 295 (1987).
[46] L. G. Stanton and M. S. Murillo, Ionic transport in high-energy-density matter, Phys. Rev. E **93**, 043203 (2016).
[47] H.-K. Chung, M. Chen, W. Morgan, Y. Ralchenko, and R. Lee, Flychk: Generalized population kinetics and spectral model for rapid spectroscopic analysis for all elements, High Energy Density Phys. **1**, 3 (2005).
[48] T. J. Callow, E. Kraisler, and A. Cangi, Improved calculations of mean ionization states with an average-atom model, Phys. Rev. Res. **5**, 013049 (2023).
[49] O. Ciricosta, S. M. Vinko, H.-K. Chung, B.-I. Cho, C. R. D. Brown, T. Burian, J. Chalupský, K. Engelhorn, R. W. Falcone, C. Graves, V. Hájková, A. Higginbotham, L. Juha, J. Krzywinski, H. J. Lee, M. Messerschmidt, C. D. Murphy, Y. Ping, D. S. Rackstraw, A. Scherz *et al.*, Direct measurements of the ionization potential depression in a dense plasma, Phys. Rev. Lett. **109**, 065002 (2012).
[50] D. Frenkel and B. Smit, Free energy calculations, in *Understanding Molecular Simulation (Second Edition)*, edited by D. Frenkel and B. Smit, 2nd ed. (Academic Press, San Diego, 2002), Chap. 7, pp. 167–200.
[51] L. M. Fraser, W. M. C. Foulkes, G. Rajagopal, R. J. Needs, S. D. Kenny, and A. J. Williamson, Finite-size effects and Coulomb interactions in quantum Monte Carlo calculations for homogeneous systems with periodic boundary conditions, Phys. Rev. B **53**, 1814 (1996).
[52] D. C. Rapaport, *The Art of Molecular Dynamics Simulation*, 2nd ed. (Cambridge University Press, Cambridge, 2004).
[53] H. G. Petersen, Accuracy and efficiency of the particle mesh Ewald method, J. Chem. Phys. **103**, 3668 (1995).
[54] K. Wünsch, J. Vorberger, and D. O. Gericke, Ion structure in warm dense matter: Benchmarking solutions of hypernetted-chain equations by first-principle simulations, Phys. Rev. E **79**, 010201(R) (2009).
[55] J. Vorberger and D. Gericke, Effective ion–ion potentials in warm dense matter, High Energy Density Phys. **9**, 178 (2013).
[56] A. P. Thompson, H. M. Aktulga, R. Berger, D. S. Bolintineanu, W. M. Brown, P. S. Crozier, P. J. in 't Veld, A. Kohlmeyer, S. G. Moore, T. D. Nguyen, R. Shan, M. J. Stevens, J. Tranchida, C. Trott, and S. J. Plimpton, LAMMPS - a flexible simulation tool for particle-based materials modeling at the atomic, meso, and continuum scales, Comput. Phys. Commun. **271**, 108171 (2022).
[57] S. Kumar, A. J. Poser, M. Schöttler, U. Kleinschmidt, W. Dietrich, J. Wicht, M. French, and R. Redmer, Ionization and transport in partially ionized multicomponent plasmas: Application to atmospheres of hot jupiters, Phys. Rev. E **103**, 063203 (2021).
[58] T. C. Beutler, A. E. Mark, R. C. van Schaik, P. R. Gerber, and W. F. van Gunsteren, Avoiding singularities and numerical instabilities in free energy calculations based on molecular simulations, Chem. Phys. Lett. **222**, 529 (1994).
[59] A. de Ruiter, D. Petrov, and C. Oostenbrink, Optimization of alchemical pathways using extended thermodynamic integration, J. Chem. Theory Comput. **17**, 56 (2021).
[60] F. Figueirido, G. S. D. Buono, and R. M. Levy, On finite-size effects in computer simulations using the ewald potential, J. Chem. Phys. **103**, 6133 (1995).
[61] J. M. Caillol, Numerical simulations of Coulomb systems: A comparison between hyperspherical and periodic boundary conditions, J. Chem. Phys. **111**, 6528 (1999).
[62] J. M. Caillol and D. Gilles, Monte carlo simulations of the Yukawa one-component plasma, J. Stat. Phys. **100**, 933 (2000).
[63] Z. A. Moldabekov, T. Dornheim, and M. Bonitz, Screening of a test charge in a free-electron gas at warm dense matter and dense non-ideal plasma conditions, Contrib. Plasma Phys. **62**, e202000176 (2022).
[64] T. Gawne, T. Campbell, A. Forte, P. Hollebon, G. Perez-Callejo, O. S. Humphries, O. Karnbach, M. F. Kasim, T. R. Preston, H. J. Lee, A. Miscampbell, Q. Y. van den Berg, B. Nagler, S. Ren, R. B. Royle, J. S. Wark, and S. M. Vinko, Investigating mechanisms of state localization in highly ionized dense plasmas, Phys. Rev. E **108**, 035210 (2023).
[65] T. Gawne, S. M. Vinko, and J. S. Wark, Quantifying ionization in hot dense plasmas, Phys. Rev. E **109**, L023201 (2024).
[66] M. Bethkenhagen, B. B. L. Witte, M. Schörner, G. Röpke, T. Döppner, D. Kraus, S. H. Glenzer, P. A. Sterne, and R. Redmer, Carbon ionization at gigabar pressures: An *ab initio* perspective on astrophysical high-density plasmas, Phys. Rev. Res. **2**, 023260 (2020).
[67] J. Clérouin, A. Blanchet, C. Blancard, G. Faussurier, F. Soubiran, and M. Bethkenhagen, Equivalence between pressure- and structure-defined ionization in hot dense carbon, Phys. Rev. E **106**, 045204 (2022).
[68] G. Ecker and W. Kröll, Lowering of the ionization energy for a plasma in thermodynamic equilibrium, Phys. Fluids **6**, 62 (1963).
[69] H. R. Griem, High-density corrections in plasma spectroscopy, Phys. Rev. **128**, 997 (1962).
[70] A. Y. Potekhin and G. Chabrier, Equation of state of fully ionized electron-ion plasmas. II. extension to relativistic densities and to the solid phase, Phys. Rev. E **62**, 8554 (2000).
[71] N. F. Carnahan and K. E. Starling, Equation of state for nonattracting rigid spheres, J. Chem. Phys. **51**, 635 (1969).